Effects of the equilibrium model on impurity transport in tokamaks

A Skyman, L Fazendeiro, D Tegnered, H Nordman, J Anderson and P Strand

Department of Earth and Space Sciences, Chalmers University of Technology, SE-412 96 Gothenburg, Sweden

E-mail: `andreas.skyman@chalmers.se`, `luisfa@chalmers.se`

Abstract. Gyrokinetic simulations of ion temperature gradient mode and trapped electron mode driven impurity transport in realistic tokamak geometry are presented and compared with results using simplified geometries. The gyrokinetic results, obtained with the GENE code in both linear and non-linear mode, are compared with data and analysis for a dedicated impurity injection discharge at JET. The impact of several factors on heat and particle transport are discussed, lending special focus to tokamak geometry and rotational shear. To this end, results using $s - \alpha$ and concentric circular equilibria are compared to results with magnetic geometry from a JET-experiment. To further approach experimental conditions, non-linear gyrokinetic simulations are performed with collisions and a carbon background included.

The impurity peaking factors, computed by finding local density gradients corresponding to zero particle flux, are discussed. The impurity peaking factors are seen to be reduced by a factor of ~ 2 in realistic geometry compared to the simplified geometries, due to a reduction of the convective pinch. It is also seen that collisions reduce the peaking factor for low Z impurities, while increasing it for high charge numbers, which is attributed to a shift in the transport spectra towards higher wave-numbers with the addition of collisions. With the addition of roto-diffusion, an over-all reduction of the peaking factors is observed, but this decrease is not sufficient to explain the flat carbon profiles seen at JET.

1. Introduction

Impurity transport is a matter of crucial relevance for Tokamak fusion plasmas [1–32] due to the contribution of impurities to radiation losses and plasma fuel dilution. The impurities can originate either from the sputtering of wall and divertor materials or from deliberate impurity injection in order to reduce power load. The impurities in a tokamak thus cover a large range in charge number Z, making it necessary to study the scaling of impurity transport with Z. This is even more relevant after the installation of the new ITER-like wall at JET [33], with its beryllium wall and tungsten divertor. In addition, a typical plasma discharge already has such a low particle density, that even a modest amount of impurities can greatly dilute the plasma, thereby reducing the power output. Since most impurity sources are located at the edge of the tokamak, the resulting impurity profile in the core of a given discharge will depend on the balance between diffusive and advective processes.

It is well known empirically that shaping of the plasma has a beneficial effect on energy confinement, the Troyon limit and the Greenwald density limit. For example, elongation (κ) is one of the factors considered in empirical scaling laws (e.g. [34]) of the energy confinement time. Only in recent years, however, has the impact of the geometric configuration on micro-turbulence been rigorously ascertained, e.g. from simulations of the gyrokinetic equations [35–39].

It has been observed that the heat-flux scales with elongation at fixed average temperature gradients, and that shaping effects enhance residual zonal flows, thus increasing the nonlinear critical temperature gradient [36]. Elongation has been seen to be the dominant effect on micro-turbulence on ion temperature gradient (ITG) and trapped electron (TE) drift-wave instabilities, compared with e.g. triangularity, up–down asymmetry and Dimits shift [38]. However, in spite of these results, the effects of the equilibrium model on impurity transport has not been studied in any detail.

Previous work in this area includes [21–23], in which the impurity transport in a dedicated impurity injection experiment at JET was studied using $s-\alpha$ geometry. It was shown that the profile steepness parameter of the injected impurities was qualitatively reproduced by the simulations. On the other hand, a discrepancy was found for the background carbon profile which was too steep at mid radius compared to the experimental profile.

In the present study, an experimental equilibrium is used and compared with results using simpler $s-\alpha$ and circular equilibria [37]. Since the impurity profile is a result of a balance between diffusion and advection, where the main advective term is the inward curvature pinch, a strong dependence on the equilibrium model may be expected. In addition, a more realistic physics description, including the effects of rotational shear on the instabilities and impurity transport (roto-diffusion), is investigated using gyrokinetic simulations. Realistic non-linear gyrokinetic simulations are performed taking into account collisionality, and the presence of a 2%C background, consistent with the conditions applying for an impurity injection experiment at JET.

The paper is organised as follows. Section 2 describes the gyrokinetic simulations performed, and the fundamental concepts of impurity transport. Section 2.2 describes the particular JET discharge considered. In Section 3, results for the the eigenvalues, turbulent fluctuation levels and transport are presented, along with a discussion on the scaling of the impurity peaking factor with impurity charge Z for the various models considered. A conclusion then follows in Section 4.

2. Background

2.1. Gyrokinetic model

The gyrokinetic simulations in this study were performed using the gyrokinetic turbulence code GENE‡ [40, 41] where a flux–tube domain was considered. This is an Eulerian–type code (i.e., employing a fixed grid in phase space), which allows for arbitrarily long simulation times. Both quasi- and nonlinear simulations including kinetic ions and electrons, and at least one impurity species were performed. All impurities were treated as fully kinetic species with low concentrations. For studying the effects of collisions, we considered the GENE implementation of the Landau–Boltzmann type collision operator [41].

For the simulation domain, all three geometries used a flux tube with periodic boundary conditions in the perpendicular plane. The nonlinear simulations were performed using a $96 \times 96 \times 32$ grid in the normal, bi-normal, and parallel spatial directions respectively; in the perpendicular and parallel momentum directions, a 12×48 grid was used. For the linear and quasilinear computations, a typical resolution was 12×32 grid points in the normal and parallel directions, with 12×64 grid points in momentum space. To validate the choice of resolutions, convergence tests for mode structure and spectra were performed.

The nonlinear simulations were typically run up to $t = 600 \, a/c_\mathrm{s}$ for the experimental geometry scenario, where a represents minor radius and $c_\mathrm{s} = \sqrt{T_e/m_i}$. For the "full scenario," in which a 2%C background and collisions were both present, the simulation time was instead $t \approx 450 \, a/c_\mathrm{s}$. This shorter time span is due to the much more computationally intensive nature of the second scenario, by a factor of ~ 2–3. The increased numerical cost was mainly due to collisions, though in part also due to the addition of the 2%C background.

2.2. Experimental profiles and parameters

The physical parameters used in the simulations are presented in table. 1 and were chosen so as to be consistent with the experimental values taken from the JET database for discharge #67330. This was previously analysed in [21], where the $s-\alpha$ geometry model was used. The discharge was part of an impurity-dedicated set of discharges with low MHD activity [32]. In these, extrinsic impurities (Ne, Ar and Ni) were injected via laser
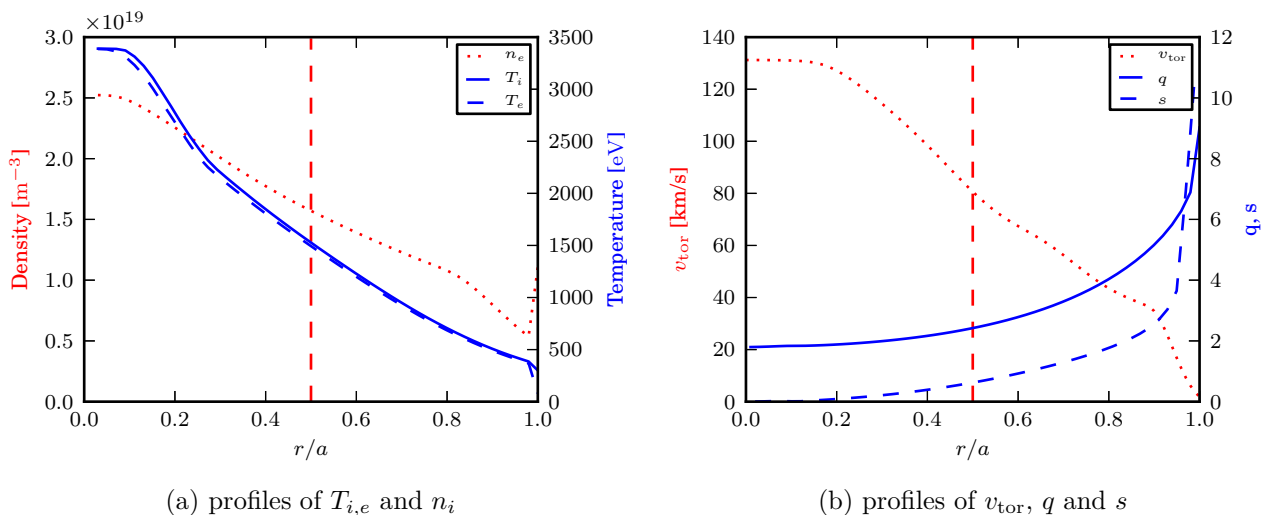
‡ `http://www.ipp.mpg.de/~fsj/gene/`

(a) profiles of $T_{i,e}$ and n_i

(b) profiles of v_{tor}, q and s

Figure 1: (colour online) Radial profiles of the background parameters for JET discharge #67730 at $t = 47.5\,\text{s}$. The simulations were performed at mid radius ($r/a = 0.5$; indicated).

ablation and gas injection. Diffusivity D_Z and convective velocity V_Z were determined by matching spectroscopic data with results obtained from predictive transport codes (see [21] and in particular Fig. 4). Profiles of density and temperature for the discharge are shown in figure 1a.

For the present study, the parameters used, including the MHD equilibrium (from now on referred to as "experimental geometry"), were taken extracted at mid radius ($r/a = 0.5$) at 48 s. The main quantities of interest were elongation $\kappa = 1.37$, triangularity $\delta = 0.044$, and the fraction of trapped particles $f_t = 0.55$. The toroidal magnetic field intensity on the axis was $B = 3\,\text{T}$, the major radius of the tokamak $R = 3\,\text{m}$, electron temperature $T_e = 1.55\,\text{k eV}$ and plasma $\beta = 8\pi n_e T_e/B^2 = 1.28 \times 10^{-3}$, and the normalised gradient of β $\alpha = -q^2 R \mathrm{d}\beta/\mathrm{d}r = 0.1026$. The safety factor in the discharge was $q = 2.2$ at the considered radius, obtained from EFIT. The collisionality was $\nu_{ei} = 0.07\,c_\mathrm{s}/R$ ($\nu_c = 0.28 \times 10^{-3}$ in GENE). Effects of purely toroidal rotation were included through the $\boldsymbol{E} \times \boldsymbol{B}$ shearing rate. The normalised gradient scale lengths are defined as $R/L_{n_j} = -(R/n_j)(\mathrm{d}n_j/\mathrm{d}r)$ and $R/L_{T_j} = -(R/T_j)(\mathrm{d}T_j/\mathrm{d}r)$ where R is the major radius of the tokamak. For the realistic equilibria, the gradients were rescaled to the minor radius with $a = \sqrt{2\Phi_\mathrm{s}/B} = 1.26\,\text{m}$, where Φ_s is the toroidal flux at the last closed flux surface. In the considered discharge, the Mach number was $M = 0.21$, leading to $\gamma_{\boldsymbol{E}\times\boldsymbol{B}} = -\frac{r}{q}\frac{1}{a}\frac{\partial v_{\text{tor}}}{\partial r} = 0.1\,c_\mathrm{s}/R$, with the toroidal velocity profile ($v_{\text{tor}}(r)$) as in figure 1b, evaluated at mid radius. Hence, we only consider the effect of flow shear in the limit where the flow is small, neglecting effects of centrifugal and Coriolis forces. These may, however, be important for heavier impurities [9].

Table 1: Parameters for gyrokinetic simulations

T_i/T_e:	1.02
β:	1.28×10^{-3}
s:	0.75
q:	2.20
$\varepsilon = r/R$:	0.17
α:	0.126
κ:	1.37
δ:	0.044
$k_\theta \rho_\mathrm{s}$:	0.2–0.6
n_e, $n_i + Z\, n_Z$:	$1.0 \cdot 10^{19}\,\mathrm{m}^{-3}$
n_Z *(trace)*:	$10^{-6} \cdot 10^{19}\,\mathrm{m}^{-3}$
Z:	2–74
$R/L_{n_{i,e}}$:	2.7
R/L_{T_i}, R/L_{T_Z}:	5.6
R/L_{T_e}:	5.6
ν_c:	$0,\ 0.28 \times 10^{-3}$
$\gamma_{\boldsymbol{E} \times \boldsymbol{B}}$:	0–0.6
T_e:	$1.55\,\mathrm{k\,eV}$
B:	$3.04\,\mathrm{T}$

2.3. Magnetic equilibrium

The gyrokinetic simulations were performed in three different geometries: $s - \alpha$, concentric circular [37] and an MHD equilibrium calculated for the JET-discharge #67330 from EFIT data using the the TRACER code (see [35] for details on the geometry implementation). A cross section of the experimental magnetic equilibrium is shown in figure 2. For the parameters under consideration, α is fairly small ($\alpha = 0.1026$), meaning that the $s - \alpha$ and circular model should be near equivalent. The $s - \alpha$ model, however, suffers from inconsistencies of the order $\varepsilon = a/R$ in its standard implementation [35, 37, 38]. Supplementary simulations using circular geometry were therefore performed, in order to better differentiate between effects of magnetic geometry and effects due to the inconsistent $s - \alpha$ metric.

2.4. Impurity transport

For trace impurities, equation (4) can be uniquely written [21] as a linear function of ∇n_Z, offset by a convective velocity or "pinch" V_Z:

$$\Gamma_Z = -D_Z \nabla n_Z + n_Z V_Z \Leftrightarrow \frac{R\Gamma_Z}{n_Z} = D_Z \frac{R}{L_{n_Z}} + R V_Z, \tag{1}$$
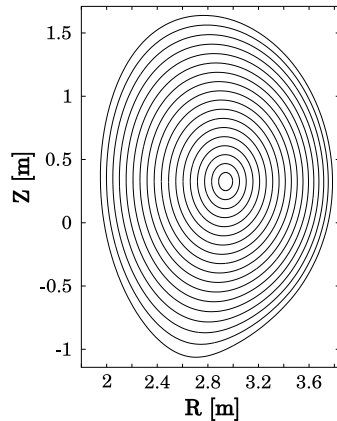
Figure 2: Cross section of the magnetic equilibrium, for JET discharge #67730.

where D_Z is the impurity diffusion coefficient, and V_Z is the impurity convective velocity, which includes roto-diffusion in the gyrokinetic treatment. Both D_Z and V_Z are independent of ∇n_Z in the trace impurity limit [16].

In the core of a steady-state plasma with fuelling from the edge (i.e. in the absence of particle sinks or sources in the core), the impurity flux Γ_Z will go to zero. Since the gradient is a measure of how peaked the impurity density profile is, the gradient of zero impurity flux is referred to as the impurity peaking factor (PF). Inserting $R/L_{n_Z} = PF$ into the linearised equation (1), it can be seen that the peaking factor quantifies the balance between convective and diffusive impurity transport:§

$$PF = -\frac{R V_Z}{D_Z}. \tag{2}$$

Specifically, the sign of the peaking factor is determined by the sign of the pinch, meaning that $PF > 0$ is indicative of a net inward impurity pinch, giving a peaked impurity profile. Conversely, if $PF < 0$ the net impurity pinch is outward, leading to a hollow impurity profile (also called *flux reversal*). For trace impurities, equation (1) is linear in R/L_{n_Z}, and the peaking factor is found by calculating the impurity particle flux (Γ_Z) for a range of R/L_{n_Z} and solving equation (1) for zero flux. For non-trace species, the D_Z and V_Z depend on R/L_{n_Z}, and the peaking factor has to be found by explicitly seeking the gradient yielding zero particle flux.

Much of the observed difference between the TE and ITG mode dominated cases can be understood from the convective velocity V_Z in equation (1). To lowest order in Z^{-1}, the pinch contains two terms that depend on Z [16]:

- thermal diffusion (thermopinch):
    - $V_{\nabla T_Z} \sim \frac{1}{Z}\frac{R}{L_{T_Z}}\omega_r,$
    - inward for TE mode ($V_{\nabla T_Z} < 0$), outward for ITG mode ($V_{\nabla T_Z} > 0$),

§ this definition is closely related to the *Péclet number* [42, 43]

- parallel impurity compression:
    - $V_{\parallel,Z} \sim \frac{Z}{A_Z} k_{\parallel}^2 \sim \frac{Z}{A_Z q^2} \approx \frac{1}{2q^2}$,
    - outward for TE mode $\left(V_{\parallel_Z} > 0 \right)$, inward for ITG mode $\left(V_{\parallel_Z} < 0 \right)$.

Here $1/k_{\parallel}$ represents the wavelength of the parallel structure of the turbulence. Due to the ballooning character of the modes considered, this is proportional to the safety factor (q). In addition, the convective velocity contains the curvature pinch, which to lowest order is independent of the impurity charge [21].

The Z dependence in the parallel impurity compression is expected to be weak, since the mass number is approximately $A_Z \approx 2Z$ for an impurity species with charge Z, and for the high q considered, this term is expected to be small compared to the other pinch contributions. The thermodiffusive contribution, however, can dominate the transport for low Z impurities (such as the Helium ash). For lower charge numbers, the second order correction to the thermal pinch can become important:

$$V_T \sim \left(\omega_r \frac{T_Z}{T_e Z} - \frac{7}{4} \left(\frac{T_Z}{T_e Z} \right)^2 \right) \frac{R}{L_{T_Z}}, \tag{3}$$

where the second order term is inward, independent of the mode direction, and finite Larmor-radius effects have been neglected [16, 21, 44, 45].

The direction of the contributions to the pinch are governed mainly by the considered mode's direction of rotation, which in the considered cases has a different sign for TE and ITG modes [45]. Expanding the convective velocity in (1) into thermal diffusion and "pure convection",

$$\Gamma_Z = -D_Z \nabla n_Z + n_Z \left(D_{T,Z} \nabla T_Z + V_{p,Z} \right), \tag{4}$$

their relative contributions to the total peaking factor can be uniquely determined for trace impurities, using the method described in e.g. [46]. Here $V_{p,Z}$ includes the parallel compression and curvature pinches. In the presence of sheared toroidal rotation (v_ϕ), these terms are joined by a roto-diffusive term, which is proportional to $\mathrm{d}v_\phi/\mathrm{d}r$.

3. Results and discussion

3.1. Background turbulence and transport

3.1.1. Linear eigenvalue spectra Using GENE, the linear eigenvalues in the studied geometries were calculated at mid-radius of JET L-mode discharge #67330 for a range of different wave numbers. The resulting spectra are compared in figure 3. The results in figure 3a show an overall destabilisation and shift toward higher $k_\theta \rho_s$ when moving from $s - \alpha$ to more realistic geometries, consistent with the results reported in [37, 47]. For triangularity of the same order as the experimental value ($\delta = 0.044$), the effect on the eigenvalues of δ was found to be minute, and it is therefore surmised that the elongation is the main factor behind the the observed results.
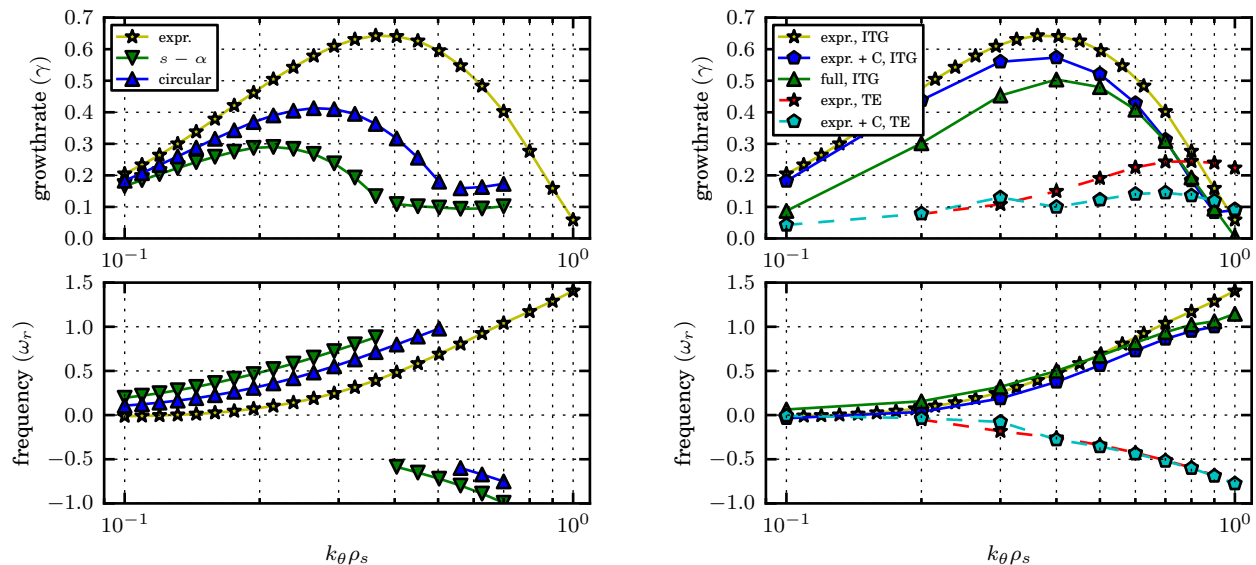
(a) eigenvalue spectra for different geometry models

(b) eigenvalue spectra in experimental geometry with added effects

Figure 3: (colour online) Growthrate spectra for $s - \alpha$, circular and experimental magnetic equilibrium for an ITG mode dominated case with JET-like parameters (3a), and for the experimental equilibrium with added degrees of realism (3b). For the second figure, *expr.* represents full geometry case with no added effects, in *expr.+C* a background of $2\%C$ was added, and in *full* collisions are added. The last case corresponds to the "full-scenario" NL runs in figure 7b. Parameters are presented in table. 1.

Adding more realism in the form of collisions and a 2% carbon background, in accordance with the "full scenario" considered in the nonlinear runs, both have a stabilising effect, as can be seen in figure 3b. The figure also shows that the stabilising effect is larger for the addition of collisions than for the carbon background, in particular for lower values of $k_\theta \rho_s$, where most of the transport normally occurs. In the second figure, the spectra for the ITG mode is supplemented with those of the sub-dominant TE mode, except in the full scenario, where it is completely stabilised, with $\gamma < 0$ for the wave-numbers considered.

The effects of sheared toroidal rotation on the ITG growth rate in the circular and experimental equilibrium are shown in figure 4. Both the stabilising perpendicular velocity shear and the destabilising parallel shearing rate are included. For the value of q considered, the mode is destabilised with increasing $\gamma_{E \times B}$. This is because the stabilising component is proportional to $1/q$, wherefore the destabilising effect dominates in the present case [48]. The shearing rate in the considered JET experiment (marked in the figure) is, however, too small to have a significant impact on the mode growth, and is left out of the nonlinear treatment below.
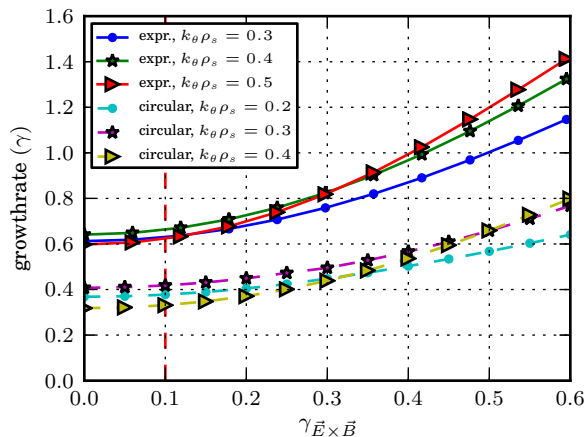
Figure 4: (colour online) Scaling of ITG growthrate with $\boldsymbol{E} \times \boldsymbol{B}$ shearing rate. The experimental shearing rate has been indicated (vertical dashed line).

3.1.2. Nonlinear transport and fluctuation levels   By comparing the transport levels for the different geometries, the difference in the turbulence can be assessed qualitatively. Time series and wave-number spectra of heat and particle flux (Q and Γ respectively) for the main ions were produced from nonlinear GENE simulations. The results are presented in figure 5.

As can be seen in figures 5a and 5b, the turbulent fluctuation level is increased when moving from $s - \alpha$ to realistic magnetic geometry. The same trend holds true for the spectra in figures 5c and 5d. Simulations using circular geometry [35, 37] place both the spectra and time series between the $s - \alpha$ and experimental case without collisions. This is consistent with the linear eigenvalues in figure 3, and with the results reported in [37]. With the addition of collisions and background carbon, the fluctuation levels are brought down, due to a general reduction of the turbulence, as seen in the the eigenvalue spectra figure 3b. The particle flux (Γ) is more sensitive to collisions than the heat flux (Q), and therefore retains a higher fluctuation level, despite the lower growthrates.

In the case with full realism, including collisions and carbon background, the fluctuation levels are lowered to an intermediate level, consistent with higher dissipation from collisions. This is also consistent with the linear eigenvalues presented in figure 3, in which the growthrates for the "full scenario" have an intermediate value between the circular (or $s - \alpha$) and the case where only effects of realistic geometry is considered. As can be seen in figures 5a and 5b, the full case was simulated for a shorter time span, due to its larger computational cost, mainly due to the inclusion of collisions, but also in part due to the 2%C background; see Section 2.1.

We note that the global confinement time in both L-mode and H-mode plasmas are scaling favourably with elongation, opposite to the trend found here for the core transport. This is likely a result of edge physics not included in the present study [49].

In addition, the zonal flow activity was investigated for each case. However, no
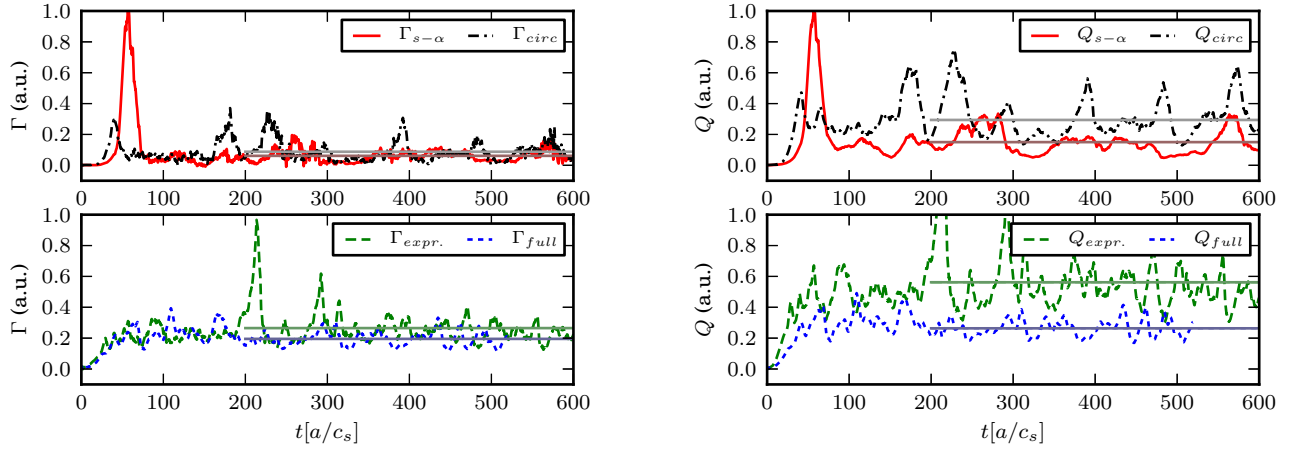
(a) timeseries of particle fluxes (Γ) with mean flux indicated

(b) timeseries of heat fluxes (Q) with mean flux indicated
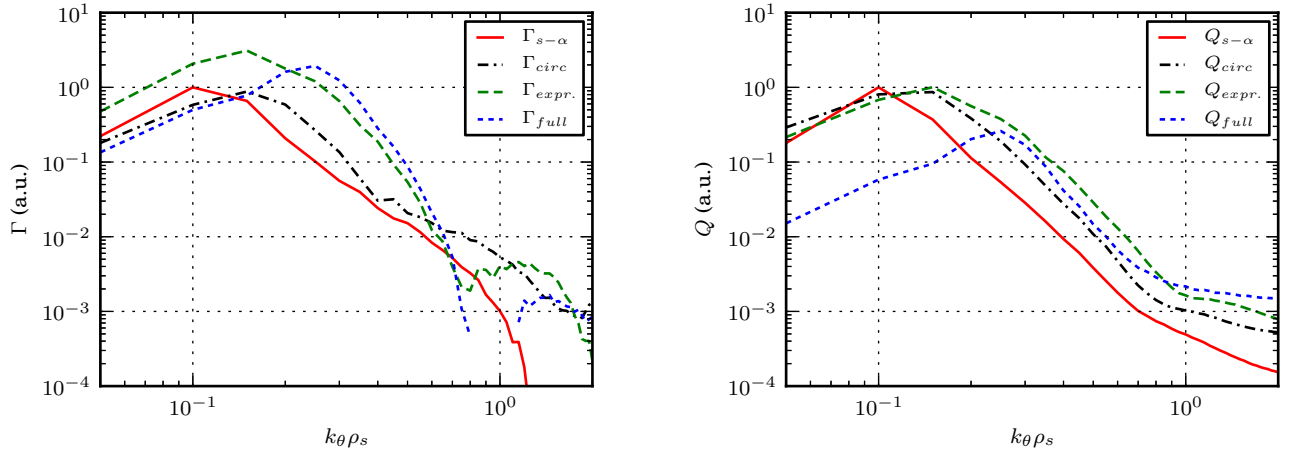
(c) spectra of particle fluxes (Γ)

(d) spectra of heat fluxes (Q)

Figure 5: (colour online) Timeseries and spectra of particle (Γ) and heat (Q) fluxes for nonlinear GENE simulations for $s - \alpha$ and circular geometry, the experimental equilibrium, and the fully realistic case, with parameters as in table. 1. Spectra show average over radial wavenumbers. The timeseries and spectra have been normalised to the maximum of the corresponding $s - \alpha$ entry. The spectra and time series show a decrease in amplitude consistent with that expected from the linear eigenvalue spectra in figure 3.
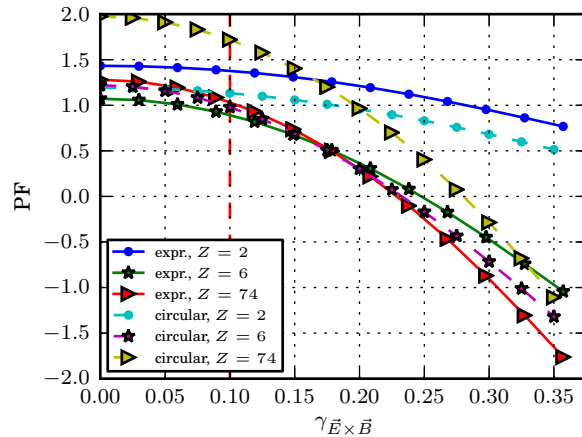
Figure 6: (colour online) Scaling of PF with $\boldsymbol{E} \times \boldsymbol{B}$ shearing rate for different impurity species in circular and shaped equilibrium for wavenumbers near the peak of the corresponding growthrate spectra ($k_\theta \rho_s = 0.3$ and $k_\theta \rho_s = 0.4$ respectively). The experimental shearing rate has been indicated (vertical dashed line).

significant differences were observed between the considered cases. The NL results can thus be explained qualitatively by the linear physics.

3.2. Impurity peaking factors

Simulations of impurity transport using a *JET*-like experimental magnetic equilibrium have been compared to simulations with $s - \alpha$ and circular geometry, using the gyrokinetic code GENE.

First, the effects sheared toroidal rotation in the different geometries is investigated The effects on the impurity peaking factors are displayed in figure 6. The peaking factors for several impurity species are shown as a function of $\gamma_{\boldsymbol{E} \times \boldsymbol{B}}$ in the experimental equilibrium. As observed, the peaking factors are reduced by the sheared rotation. This leads to a reversal of the impurity pinch for $\gamma_{\boldsymbol{E} \times \boldsymbol{B}} \gtrsim 0.23$ for all but the lightest impurities ($Z \lesssim 4$) in the experimental equilibrium. In the circular geometry the trends are the same, but the flux reversal for Tungsten ($Z = 74$) is shifted to higher rotational sharing rate ($\gamma_{\boldsymbol{E} \times \boldsymbol{B}} \gtrsim 0.28$). This effect, due to roto-diffusion, has been found to be a critical ingredient to include in order to reproduce the Boron profile in ASDEX U [50]. For the considered discharge, however, the shearing rate is small and hence it is neglected in the non-linear analysis.

Next, the effects of the geometry on the scaling with impurity charge are investigated. In figure 7a the scaling of the impurity peaking factor (PF) with impurity charge (Z) is shown, for $s - \alpha$, circular and experimental geometry. Non-linear (NL) gyrokinetic results are compared in figure 7b for added degrees of realism. Error-bars in figure 7b correspond to a conservative standard error estimate of $\pm \sigma$. This was calculated from the NL flux data, where an effective sample size was gauged for the

time series and used to estimate the error for the mean flux. This estimate was then propagated through to an error estimate for the peaking factor. The effects on the PF-scaling of adding collisions and 2%C background, consistent with the considered JET discharge, are shown in figure 7c.

For moderate to high impurity charge, weaker scalings of PF with Z were consistently observed when departing from the $s - \alpha$ equilibrium, and the level at which PF saturates for high Z was reduced in the experimental geometry case. The lower PF levels compared to $s - \alpha$ geometry can be attributed to a reduction of the convective pinch due to effects of shaping, but also due to effects of finite inverse aspect ratio (ε) effects, as discussed in Section 2.2. To separate the effects of shaping from the inconsistent ε effects in the $s-\alpha$ model, simulations using GENE's circular geometry [37] were performed. Since $\alpha \ll 1$ in the studied discharge, the difference between the results using circular and experimental equilibrium in figure 7a can attributed to shaping effects, mainly due to elongation. Further, a large increase in PF was observed for low Z impurities, most notably He impurities, in circular and experimental geometry. This is due to a reduction of the outward thermopinch in the more realistic equilibrium models, as discussed in Section 3.3.

In figure 7b non-linear results using $s - \alpha$ geometry from [21] are compared with NL gyrokinetic simulations using the experimental equilibrium for two different sets of parameters. The first NL set of runs only uses the experimental geometry, whereas the full case also includes a carbon background and collisions, but neglects effects of sheared toroidal rotation (*full* in figure 3). With the introduction of these two effects, PF is lowered for low Z and increased for high Z. As seen in the quasilinear runs, the NL GK results are lower than those predicted by the $s - \alpha$ model, though a qualitative agreement is reached in the full scenario, particularly for high Z. When comparing QL and NL results, the former show a more dramatic scaling than the latter and the QL results tend to over-estimate PF for high Z, as can be seen in figure 7c. In all models there is, as expected, a saturation of PF in the high Z limit [16, 21, 22], and the observed NL and QL impurity pinches qualitatively agree with the results in [21, 22].

Figure 7c shows the effect of adding collisions and a 2% carbon background to the PF scaling with Z, using QL gyrokinetics. The "base case" corresponds to the experimental MHD equilibrium, without any added effects (*expr.* in figure 3). In all cases $k_\theta \rho_s = 0.4$ was used, since that is the approximate value for the maximum linear growth rate, as shown in figure 3. As with the eigenvalue spectra (figure 3b), it is clear that the addition of collisions to the model has a larger impact than the addition of the 2%C background. The addition of the carbon background slightly raises PF for low Z, but the addition of collisions lowers it considerably, as well as raising PF for high charge numbers, as seen for the NL runs. These results are consistent with previous observations of the importance of impurity–main ion collisions for core impurity transport [51, 52]. We note that, although a reduction is seen in the peaking for carbon impurities in the realistic case, the flat or hollow profile seen in experiments is not reproduced. Though a further reduction is expected from roto-diffusion, nonlinear
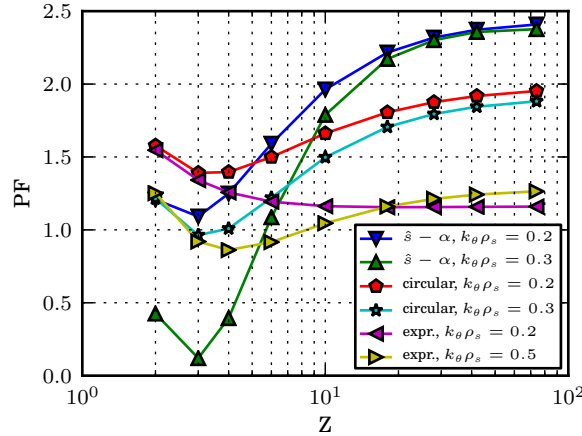
(a) comparison of $s - \alpha$, circular and experimental geometries for QL GENE
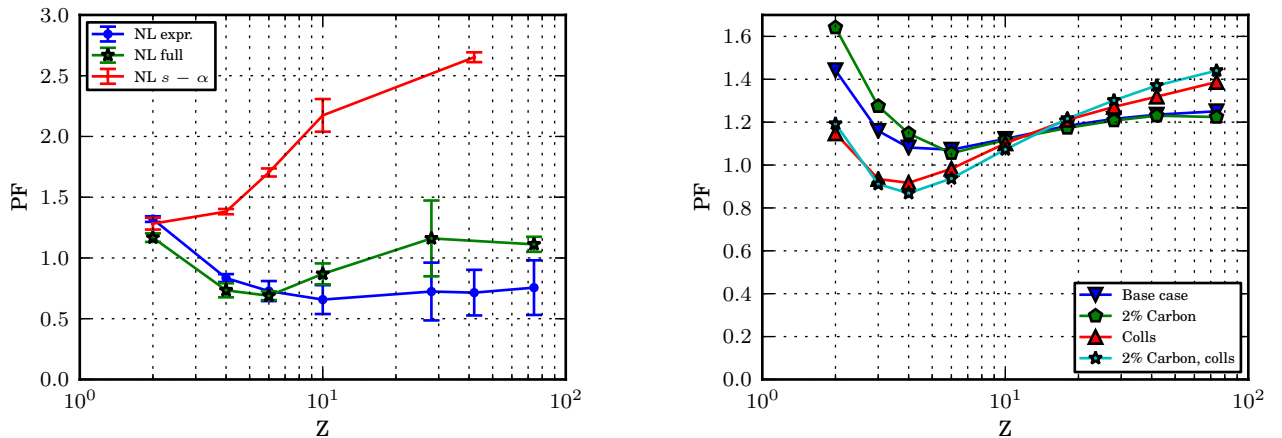
(b) comparison of NL GENE base case and full case (*expr.* and *full* in figure 3) with results for $s - \alpha$ geometry from [21]; error-bars indicate a standard error of $\pm\sigma$.

(c) effects of added realism on QL Z-scaling for $k_\theta \rho_s = 0.4$

Figure 7: (colour online) Scalings of impurity peaking factor (PF) with impurity charge number (Z) from JET discharge #67730 for $s-\alpha$, circular and experimental equilibrium. Parameters as in table. 1.

simulations of the full scenario with sheared toroidal rotation still show an inward nett transport of the background carbon.

3.3. Contributions to the impurity pinch

In order to gain more insight into the results presented in the last section, the contributions to the peaking factor were calculated using the method outlined in [46].

Figure 8 shows the effect of shaping on the thermodiffusive and convective contributions to the impurity peaking factor (equation (4)). It is seen, that the increase

in peaking factor observed for lighter impurities is mainly due to the thermopinch, where the inward second order contribution to the thermal pinch comes into dominance over the outward term (equation (3)). This effect becomes more pronounced for lower wave-numbers – especially in the shaped equilibrium – due to the lower mode frequency (figure 3). For higher Z, however, the peaking is determined by the balance of the inward convective pinch and the diffusion. This contribution is only weakly dependent on the impurity charge and wave-number, and is reduced substantially in the shaped equilibrium.

In figure 9 diffusivities and pinches obtained from NL GENE are compared with with data from [21]. From these results we note that, in contrast to the diffusivity (D_Z), the convective velocity ($|V_Z|$) is lower in the realistic equilibrium as compared to the $s - \alpha$ case, despite the corresponding increase in fluctuation levels (figure 5b). This confirms the conclusion that the main reason for the reduced peaking factors obtained in the experimental equilibrium is a reduction of the convective velocity. When comparing the collisionless shaped equilibrium with the full scenario, we note that the diffusivity is decreased, as expected from the observed decrease in fluctuation levels with the addition of collisions. For high Z, the reduction in convective velocity is similar in both cases, compared to the $s - \alpha$ equilibrium, leading to higher peaking factors in the full scenario.

When comparing the scalings for low ($k_\theta \rho_s = 0.2$) and high ($k_\theta \rho_s = 0.5$) wavenumbers in the case with shaping, it is seen that the thermal diffusion is dominated completely by the higher order terms ($\sim Z^{-2}$) in the low wavenumber case, turning from mostly outward to inward. In the full case, the NL spectrum was seen to shift toward higher wavenumbers, compared to the case with shaping but without collisions and carbon background (figure 5). The difference between the non-linear gyrokinetic results in figure 7b is therefore consistent with the interpretation that higher order terms dominate the thermal diffusion for lower wave numbers, thereby determining the shape of the peaking factor scaling.

4. Conclusions

The effects of the choice of equilibrium model on impurity transport in ITG/TE mode driven turbulence were studied using gyrokinetic simulations. Results were obtained and contrasted for the experimental MHD equilibrium and the simpler $s - \alpha$ and concentric circular geometries. These results were extended by adding degrees of realism in the physics description, such as a 2% carbon background, collisions, and sheared toridal rotation. The gyrokinetic results, obtained with the GENE code in both quasi- and non-linear mode, were compared with results from a previous study, as well as with expectations from a dedicated impurity injection L-mode discharge at JET. It is found that the different equilibria give qualitatively similar results, but with significant quantitative differences.

Linearly, a destabilisation and shift of the growthrate spectrum to higher wave numbers was seen when departing from the simpler geometries, mainly due to elongation.
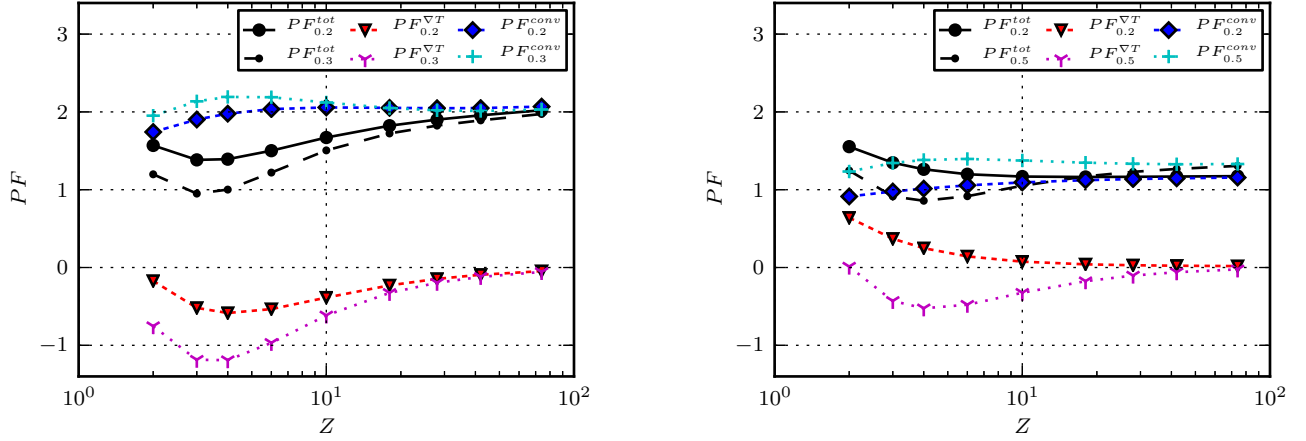
(a) contributions to the pinch for circular equilibrium   (b) contributions to the pinch for experimental equilibrium

Figure 8: (colour online) Contributions to the peaking factor ($PF_{k_\theta \rho_s}^{\text{tot}}$) from thermodiffusion ($PF_{k_\theta \rho_s}^{\nabla T}$) and pure convection ($PF_{k_\theta \rho_s}^{\text{conv}}$) as a function of impurity charge (Z). Results from QL GENE for wavenumbers as in figure 7, with and without effects of shaping ($\kappa = 1.0$, $\kappa = 1.37$).

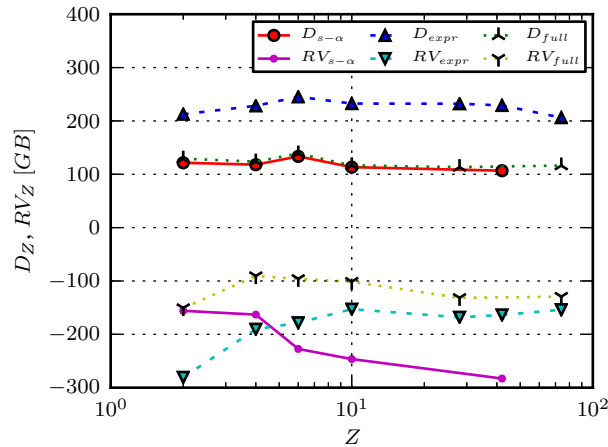
Figure 9: (colour online) Scaling of the impurity diffusivity (D_Z) and total pinch (RV_Z) with impurity charge for $s - \alpha$ geometry and experimental geometry, with and without collisions and 2%C background. Data from NL GENE simulations with standard errors 10–20% (omitted for clarity).

This resulted in larger heat and particle transport, as seen in the nonlinear simulations. The addition of collisions was seen to stabilise the spectrum and reduce transport.

The effect of sheared rotation on the mode stability and the impurity transport was studied. A weak destabilisation of the ITG mode with $\boldsymbol{E} \times \boldsymbol{B}$ shear was found. However, this was seen to be a minor contribution for experimentally feasible values of the rotational shearing rate for the considered discharge.

The impurity peaking factors (PFs), computed by finding local density gradients corresponding to zero particle flux, were derived. The peaking factor was observed to saturate at levels far below neo-classical predictions for high impurity charge numbers. The level of the saturation was considerably lowered when the experimental equilibrium was used, typically by a factor of ~ 2. Comparing the diffusivity and convective pinch velocity in the different geometries, it was found that the reduction of PF was mainly due to a reduction of the convective pinch.

By decomposing the contributions to the peaking factor into thermodiffusion and pure convection, it was seen that second order contributions to the thermal diffusion became important for low impurity charge. Whereas the first order term is proportional to ω_r, and therefore outward for ion temperature gradient modes, the second order contribution to the pinch is always inward, and therefore leads to higher PFs. This explains the more pronounced increase in peaking observed for low charge numbers in the shaped equilibria, where the real frequency is lower.

Collisions were seen to affect the impurity peaking factors considerably, lowering PF for light impurities, while increasing it for heavy impurities. It was seen, that the addition of collisions and background carbon shifted the nonlinear spectra towards higher wavenumbers, associated with higher real frequencies. Therefore, the the difference between the nonlinear results in the experimental equilibrium could be also understood through the second order term in the thermopinch, which was concluded to dominate this pinch contribution for the non-collisional case.

However, even combining the effect of collisions with the effect of geometry and rotation in the most realistic simulations, the observed peaking factor for carbon was still too large to explain the rather flat C profile observed in the experiment. One explanation for this descrepancy could lie in the sensitivity of the thermopinch to main ion and impurity temperature, and to the gradients of thereof. A moderate variation in these may bring the background carbon peaking factor down to zero, however, such a treatment is left for future studies. We also note that the treatment of rotation employed in this study neglects centrifugal and Coriolis forces, which may lower the impurity peaking further.

Acknowledgements

References

[1] Fröjdh M, Liljeström M and Nordman H 1992 *Nucl. Fusion* **32** 419

[2] Basu R, Jessen T, Naulin V and Rasmussen J J 2003 *Phys. Plasmas* **10** 2696

[3] Estrada-Mila C, Candy J and Waltz R W 2005 *Phys. Plasmas* **12** 022305

[4] Naulin V 2005 *Phys. Rev. E* **71** 015402

[5] Priego M, Garcia O E, Naulin V and Rasmussen J J 2005 *Phys. Plasmas* **12** 062312

[6] Fülöp T and Weiland J 2006 *Phys. Plasmas* **13** 112504

[7] Bourdelle C, Garbet X, Imbeaux F, Casati A, Dubuit N, Guirlet R and Parisot T 2007 *Phys. Plasmas* **14** 112501

[8] Dubuit N, Garbet X, Parisot T, Guirlet R and Bourdelle C 2007 *Phys. Plasmas* **14** 042301

[9] Camenen Y, Peeters A G, Angioni C, Casson F J, Hornsby W A, Snodin A P and Strintzi D 2009 *Phys. Plasmas* **16** 012503

[10] Fülöp T, Braun S and Pusztai I 2010 *Phys. Plasmas* **17** 062501

[11] Futatani S, Garbet X, Benkadda S and Dubuit N 2010 *Phys. Rev. Lett.* **104** 015003

[12] Hein T and Angioni C 2010 *Phys. Plasmas* **17** 012307

[13] Moradi S, Tokar M Z and Weyssow B 2010 *Phys. Plasmas* **17** 012101

[14] Fülöp T and Moradi S 2011 *Phys. Plasmas* **18** 030703

[15] Nordman H, Singh R, Fülöp T, Eriksson L G, Dumont R, Anderson J, Kaw P, Strand P, Tokar M and Weiland J 2008 *Phys. Plasmas* **15** 042316

[16] Angioni C and Peeters A G 2006 *Phys. Rev. Lett.* **96** 095003

[17] Angioni C, Carraro L, Dannert T, Dubuit N, Dux R, Fuchs C, Garbet X, Garzotti L, Giroud C, Guirlet R, Jenko F, Kardaun O J W F, Lauro-Taroni L, Mantica P, Maslov M, Naulin V, Neu R, Peeters A G, Pereverzev G, Puiatti M E, Pütterich T, Stober J, Valovič M, Valisa M, Weisen H, Zablotsky A, ASDEX Upgrade team and JET–EFDA contributors 2007 *Phys. Plasmas* **14** 055905

[18] Nordman H, Fülöp T, Candy J, Strand P and Weiland J 2007 *Phys. Plasmas* **14** 052303

[19] Angioni C, Peeters A G, Pereverzev G V, Bottino A, Candy J, Dux R, Fable E, Hein T and Waltz R E 2009 *Nucl. Fusion* **49** 055013

¶ See `http://www.c3se.chalmers.se`

[20] Fülöp T and Nordman H 2009 *Phys. Plasmas* **16** 032306

[21] Nordman H, Skyman A, Strand P, Giroud C, Jenko F, Merz F, Naulin V, Tala T and the JET–EFDA contributors 2011 *Plasma Phys. Contr. F.* **53** 105005

[22] Skyman A, Nordman H and Strand P 2012 *Phys. Plasmas* **19** 032313

[23] Skyman A, Nordman H and Strand P 2012 *Nucl. Fusion* **52** 114015

[24] Mollén A, Pusztai I, Fülöp T, Kazakov Y O and Moradi S 2012 *Phys. Plasmas* **19** 052307

[25] Moradi S, Pusztai I, Mollén A and Fülöp T 2012 *Phys. Plasmas* **19** 032301

[26] Kazakov Y O, Fülöp T and Van Eester D 2013 *Nucl. Fusion* **53** 053014

[27] Mollén A, Pusztai I, Fülöp T and Moradi S 2013 *Phys. Plasmas* **20** 032310

[28] Dux R, Neu R, Peeters A G, Pereverzev G, Mück A, Ryter F and Stober J 2003 *Plasma Phys. Contr. F.* **45** 1815

[29] Puiatti M E, Valisa M, Mattioli M, Bolzonella T, Bortolon A, Coffey I, Dux R, von Hellermann M, Monier-Garbet P, Nave M F F, Ongena J and contributors to the EFDA–JET workprogramme 2003 *Plasma Phys. Contr. F.* **45** 2011

[30] Puiatti M E, Valisa M, Angioni C, Garzotti L, Mattioli M, Carraro L, Coffey I and Sozzi C 2006 *Phys. Plasmas* **13** 042501

[31] Giroud C, Barnsley R, Buratti P, Coffey I H, von Hellermann M, Jupén C, Lawson K D, Meigs A, O'Mullane M, Whiteford A D, Zastrow K D and the JET–EFDA contributors 2007 *Nucl. Fusion* **47** 313

[32] Giroud C et al 2009 Impurity characterisation in JET operational scenarios *12th International Workshop on "H-mode Physics and Transport Barriers"* Princeton, USA URL `http://iopscience.iop.org/0029-5515/50/6`

[33] Matthews G F, Edwards P, Greuner H, Loving A, Maier H, Martens P, Philipps V, Riccardo V, Rubel M, Ruset C, Scmidt A and Villedieu E 2009 *Phys. Scr.* **2009** 014030

[34] Doyle E J et al 2007 Plasma confinement and transport *Progress in the ITER Physics Basis* vol 47 (Nucl. Fusion) chap 2, p S18

[35] Xanthopolous P and Jenko F 2006 *Phys. Plasmas* **13** 092301

[36] Belli E A, Hammett G W and Dorland W 2008 *Phys. Plasmas* **15** 092303

[37] Lapillonne X, Brunner S, Dannert T, Jolliet S, Marioni A, Villard L, Görler T, Jenko F and Merz F 2009 *Phys. Plasmas* **16** 032308

[38] Burckel A, Sauter O, Angioni C, Candy J, Fable E and Lapillonne X 2010 *J. Phys.: Conf. Ser.* **260** 012006

[39] Told D and Jenko F 2010 *Phys. Plasmas* **17** 042302

[40] Jenko F, Dorland W, Kotschenreuther M and Rogers B N 2000 *Phys. Plasmas* **7** 1904

[41] Merz F 2008 *Gyrokinetic Simulation of Multimode Plasma Turbulence* Ph.d. thesis (monography) Westfälischen Wilhelms-Universität Münster

[42] Arter W 1995 *Rep. Prog. Phys.* **58** 1

[43] Bakunin O G 2003 *Plasma Phys. Contr. F.* **45** 1909

[44] Nilsson J, Liljeström M and Weiland J 1990 *Phys. Fluids B* **2** 2568

[45] Weiland J 2000 *Collective Modes in Inhomogeneous Plasmas* (Bristol, UK: IoP Publishing)

[46] Casson F J, Peeters A G, Angioni C, Camenen Y, Hornsby W A, Snodin A P and Szepesi G 2010 *Phys. Plasmas* **17** 102305

[47] Anderson J, Nordman H and Weiland J 2000 *Plasma Phys. Contr. F.* **42** 545

[48] Barnes M, Parra F I, Highcock E G, Schekochihin A A, Cowley S C and Roach C M 2011 *Phys. Rev. Lett.* **106** 175004

[49] ITER Physics Expert Group on Confinement and Transport, ITER Physics Expert Group on Confinement Modelling and Database and ITER Physics Basis Editors 1999 Plasma confinement and transport *ITER Physics Basis* vol 39 (Nucl. Fusion) chap 2, p 2175

[50] Angioni C, McDermott R, Fable E, Fischer R, Pütterich T, Ryter F, Tardini G and the ASDEX Upgrade Team 2011 *Nucl. Fusion* **51** 023006

[51] Angioni C, Peeters A G, Jenko F and Dannert T 2005 *Phys. Plasmas* **12** 112310

[52] Moradi S, Tokar M Z, Singh R and Weyssow B 2009 *Nucl. Fusion* **49** 085007